Three-dimensional airway reopening: the steady propagation of a semi-indefinite bubble into a buckled elastic tube

Hazel, Andrew L. and Heil, Matthias

2003

MIMS EPrint: **2006.235**

Manchester Institute for Mathematical Sciences
School of Mathematics

The University of Manchester

Reports available from: http://eprints.maths.manchester.ac.uk/
And by contacting: The MIMS Secretary
School of Mathematics
The University of Manchester
Manchester, M13 9PL, UK

ISSN 1749-9097

J. Fluid Mech. (2003), *vol.* 478, *pp.* 47–70.
DOI: 10.1017/S0022112002003452 Printed in the United Kingdom

Three-dimensional airway reopening: the steady propagation of a semi-infinite bubble into a buckled elastic tube

By ANDREW L. HAZEL AND MATTHIAS HEIL

Department of Mathematics, University of Manchester, Oxford Road, Manchester M13 9PL, UK

(Received 28 February 2002 and in revised form 24 October 2002)

We consider the steady propagation of an air finger into a buckled elastic tube initially filled with viscous fluid. This study is motivated by the physiological problem of pulmonary airway reopening. The system is modelled using geometrically nonlinear Kirchhoff–Love shell theory coupled to the free-surface Stokes equations. The resulting three-dimensional fluid–structure-interaction problem is solved numerically by a fully coupled finite element method.

The system is governed by three dimensionless parameters: (i) the capillary number, $Ca = \mu U/\sigma^*$, represents the ratio of viscous to surface-tension forces, where μ is the fluid viscosity, U is the finger's propagation speed and σ^* is the surface tension at the air–liquid interface; (ii) $\sigma = \sigma^*/(RK)$ represents the ratio of surface tension to elastic forces, where R is the undeformed radius of the tube and K its bending modulus; and (iii) $A_\infty = A^*_\infty/(4R^2)$, characterizes the initial degree of tube collapse, where A^*_∞ is the cross-sectional area of the tube far ahead of the bubble.

The generic behaviour of the system is found to be very similar to that observed in previous two-dimensional models (Gaver *et al.* 1996; Heil 2000). In particular, we find a two-branch behaviour in the relationship between dimensionless propagation speed, Ca, and dimensionless bubble pressure, $p^*_b/(\sigma^*/R)$. At low Ca, a decrease in p^*_b is required to increase the propagation speed. We present a simple model that explains this behaviour and why it occurs in both two and three dimensions. At high Ca, p^*_b increases monotonically with propagation speed and $p^*_b/(\sigma^*/R) \propto Ca$ for sufficiently large values of σ and Ca. In a frame of reference moving with the finger velocity, an open vortex develops ahead of the bubble tip at low Ca, but as Ca increases, the flow topology changes and the vortex disappears.

An increase in dimensional surface tension, σ^*, causes an increase in the bubble pressure required to drive the air finger at a given speed; p^*_b also increases with A^*_∞ and higher bubble pressures are required to open less strongly buckled tubes. This unexpected finding could have important physiological ramifications. If σ^* is sufficiently small, steady airway reopening can occur when the bubble pressure is lower than the external (pleural) pressure, in which case the airway remains buckled (non-axisymmetric) after the passage of the air finger. Furthermore, we find that the maximum wall shear stresses exerted on the airways during reopening may be large enough to damage the lung tissue.

1. Introduction

A number of pulmonary diseases can cause the smaller airways of the lung to collapse and become occluded by the liquid that normally coats their interiors

(Pride & Macklem 1986; Hughes, Rosenzweig & Kivitz 1970; Macklem, Proctor & Hogg 1970). If the airways remain occluded for significant periods of time then gas exchange will be severely impaired with potentially fatal consequences. Airway collapse is facilitated by a number of mechanical factors (Halpern & Grotberg 1992), including: (i) increased lung compliance (e.g. in emphysema); (ii) an increase in the volume of fluid in the liquid lining (e.g. in asthma or pulmonary œdema); and/or (iii) increased surface tension of the liquid lining, usually caused by insufficient natural surfactant (e.g. respiratory distress syndrome).

The propagation of an air finger into the buckled fluid-filled regions is believed to reopen the airway, a phenomenon first studied by Gaver, Samsel & Solway (1990). The same mechanism also occurs at the 'first breath' when air enters the fluid-filled lungs of a newborn baby. The aim of any treatment is to ensure that the propagating air finger reopens the airways as quickly as possible, but without damaging the lungs. This is particularly important during mechanical ventilation.

Gaver *et al.* (1990) performed an experimental study to model airway reopening. They investigated the propagation of an air finger into a buckled thin-walled polyethylene tube, filled with viscous fluid. The authors determined the dependence of the propagation speed, U, upon the applied bubble pressure, p_b^*, and found that p_b^* appeared to approach a finite value as U tended towards zero. This finite value was interpreted as the minimum pressure required to initiate motion of the finger: the yield pressure.

The mechanics of airway reopening are governed by a complex three-dimensional fluid–structure interaction (a free-surface flow coupled to the deformation of an elastic tube) and are still incompletely understood, partly because all previous theoretical studies have been based on two-dimensional models. The first such study was conducted by Gaver *et al.* (1996), who modelled the airway as an infinitely long two-dimensional channel with flexible walls, subject to an imposed axial tension, T. In this model, the walls are supported by linearly elastic springs of stiffness K_{spring} with a rest length that corresponds to a channel width of $2H$. A semi-infinite bubble, under internal pressure p_b^*, propagates at a constant speed, U, into the channel, which contains a fluid of viscosity μ, and the surface tension between the air and the fluid is σ^*. The model was used to predict the bubble pressure as a function of propagation speed in the absence of inertia. Generic results are shown in figure 1, in which the bubble pressure is non-dimensionalized on the capillary scale, $p_b^*/(\sigma^*/H)$, and the capillary number, $Ca = \mu U/\sigma^*$, the ratio of viscous forces to surface-tension forces, is used as a measure of the bubble speed.

The model predicts a two-branch behaviour. At high Ca, the physically expected behaviour is observed and an increase in bubble pressure causes an increase in propagation speed. In this regime, the fluid layer appears to 'peel' the channel walls apart. Conversely, at low Ca, the behaviour changes and a decrease in bubble pressure is required to increase the propagation speed of the air finger. In this regime, a large volume of fluid is 'pushed' ahead of the bubble tip and a closed recirculation region develops in a frame of reference moving with the bubble tip. Gaver *et al.* (1996) termed the low-Ca region the 'pushing' branch and the high-Ca region the 'peeling' branch. Perhaps the most useful result, from a clinical point of view, was the prediction of a minimum pressure, p_{min}^*, where the two branches connect and below which there are no steady solutions.

Extensions to the two-dimensional airway-reopening model have been considered by a number of authors: Yap & Gaver (1998) investigated the effects of surfactant on the system; Heil (2000) explored the rôle of fluid inertia; Horsburgh (2000)

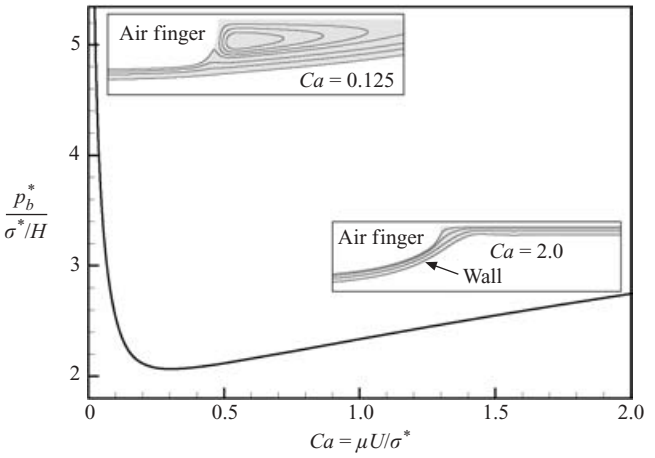

FIGURE 1. Bubble pressure vs. capillary number for the two-dimensional model of Gaver *et al.* (1996). The data were generated by Heil's (2000) numerical code using the material parameters $\eta = T/\sigma^* = 100$ (dimensionless wall tension) and $\Gamma = K_{\text{spring}} H^2/\sigma^* = 0.5$ (dimensionless wall stiffness). Inset figures illustrate generic channel shapes and streamlines on the two branches; only one half of the domain is shown.

determined the effect of wall permeability, motivated by the first-breath scenario. He also examined the stability of the 'pushing' branch and showed that it is unstable if the flow is driven by a prescribed pressure. More recently, Jensen *et al.* (2002) have developed an asymptotic description of the 'peeling' branch.

While the two-dimensional models appear to capture many features of airway reopening, a number of potentially important three-dimensional effects have been neglected. In particular, the flow and the wall deformation in the region close to the tip of the air finger will be inherently three-dimensional. A more fundamental shortcoming of the existing two-dimensional models is that a change in transmural pressure, $\mathscr{P}^*_{\text{tm}}$, defined to be the external (pleural) minus the internal (fluid) pressure, in the fluid-filled region is equivalent to a rescaling of the transverse lengthscale. In three dimensions, the undeformed airway radius sets a natural transverse lengthscale and the transmural pressure (or, equivalently, the initial degree of collapse) becomes an important parameter in the problem.

This paper is an extension of the previous work of Heil (2000) and represents a fully consistent model of three-dimensional airway reopening. The aim of the study is to determine the relationship between the (applied) bubble pressure and the (resulting) propagation speed under the influence of the system parameters.

2. The model

We consider the steady motion of an inviscid air finger into a fluid-filled elastic tube of infinite length, undeformed midplane radius R, wall thickness h, Poisson's ratio ν and Young's modulus E. Far ahead of the finger tip, the fluid is at rest and the tube is in a uniformly buckled state, characterized by its cross-sectional area, A^*_∞. The air finger is driven by an internal bubble pressure, p^*_b, and propagates at a constant speed, U. After passage of the finger tip, the tube reopens and a film of fluid is deposited on the tube walls. The fluid is assumed to be Newtonian and incompressible with viscosity μ and the surface tension at the air–liquid interface is assumed to be a constant, σ^*.

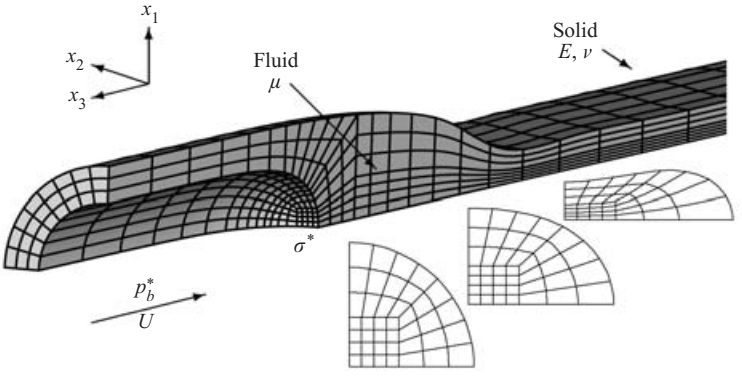

FIGURE 2. An inviscid air finger propagates at a constant speed, U, into a buckled elastic tube (Young's modulus E and Poisson's ratio ν) initially filled with a fluid of viscosity μ. The internal pressure of the air finger is p_b^* and the (constant) surface tension at the air–liquid interface is σ^*. Illustrative cross-sections through the fluid domain are shown, demonstrating the deformation of the finite element mesh in response to changes in the position of the wall and the air–liquid interface; only one quarter of the domain is shown.

The presence of natural surfactant in the lung could result in a non-uniform surface tension along the interface, see e.g. Yap & Gaver (1998) and Ghadiali, Halpern & Gaver (2001), but this effect is neglected in the present work.

The problem is formulated in dimensionless Cartesian coordinates, $\boldsymbol{x} = (x_1, x_2, x_3) = \boldsymbol{x}^*/R$. Hereinafter, an asterisk is used to indicate dimensional quantities, as opposed to their dimensionless equivalents. The x_3-coordinate is chosen to vary along the axis of the tube, with the finger propagating in the negative x_3-direction, and x_1, x_2 are the transverse coordinates, see figure 2.

2.1. *Fluid equations*

The fluid velocity scale is chosen to be the propagation speed of the finger, $\boldsymbol{u} = \boldsymbol{u}^*/U$ and the internal fluid pressure is scaled on the viscous scale, $p = p^*/(\mu U/R)$. The effects of fluid inertia are neglected and hence the capillary number, $Ca = \mu U/\sigma^*$, is the only dimensionless grouping in the fluid equations.

In a frame moving with the (constant) velocity of the bubble, U, the flow is governed by the dimensionless, steady Stokes equations

$$-\frac{\partial p}{\partial x_i} + \frac{\partial}{\partial x_j}\left(\frac{\partial u_i}{\partial x_j} + \frac{\partial u_j}{\partial x_i}\right) = 0, \tag{1a}$$

and the continuity equation

$$\frac{\partial u_i}{\partial x_i} = 0, \tag{1b}$$

where $i, j = 1, 2, 3$ and the Einstein summation convention is used.

There are two boundary conditions on the free surface:

$$u_i n_i = 0 \quad \text{(non-penetration)}, \tag{2a}$$

$$-pn_i + \left(\frac{\partial u_i}{\partial x_j} + \frac{\partial u_j}{\partial x_i}\right) n_j + \frac{1}{Ca}\kappa n_i = -p_b n_i \quad \text{(dynamic boundary condition)}. \tag{2b}$$

$\boldsymbol{n}$ is the unit normal to the free surface (directed out of the fluid), $\kappa = \kappa^* R$ is the dimensionless (first) curvature of the surface, the sum of the principal curvatures, and p_b is

the dimensionless internal bubble pressure. Finally, we fix the bubble tip at the origin:

$$(x_3)_{\text{tip}} = 0. \tag{2c}$$

2.2. *Wall equations*

We use geometrically nonlinear Kirchhoff–Love shell theory to model the deformation of the elastic tube. In this theory, the deformation of the shell is completely specified by the displacements of its midplane, $\boldsymbol{v} = \boldsymbol{v}^*/R$. Lagrangian coordinates, $\xi^\alpha = \xi^{*\alpha}/R$, where $\alpha = 1, 2$, are introduced to parameterize the midplane, and time is non-dimensionalized by $t = t^*U/R$. Changing to a frame moving with the bubble tip is equivalent to formulating the problem in Lagrangian travelling-wave coordinates, $\zeta^1 = \xi^1 + t$, $\zeta^2 = \xi^2$. The location of the undeformed midplane is then given by the position vector, $\boldsymbol{r} = \boldsymbol{r}^*/R$,

$$\boldsymbol{r} = (\cos(\zeta^2), \sin(\zeta^2), \zeta^1), \quad \zeta^1 \in [-\infty, \infty], \quad \zeta^2 \in [0, 2\pi]. \tag{3}$$

The base vectors of the undeformed midplane are $\boldsymbol{a}_\alpha = \boldsymbol{r}_{,\alpha}$, where the comma denotes partial differentiation with respect to ζ^α, and the covariant midplane metric tensor is $a_{\alpha\beta} = \boldsymbol{a}_\alpha \cdot \boldsymbol{a}_\beta$, with determinant $a = a_{11}a_{22} - a_{12}a_{21}$. We also define a curvature tensor, $b_{\alpha\beta} = \boldsymbol{n} \cdot \boldsymbol{a}_{\alpha,\beta}$, where $\boldsymbol{n} = \boldsymbol{a}_1 \times \boldsymbol{a}_2/|\boldsymbol{a}_1 \times \boldsymbol{a}_2|$ is the unit normal to the midplane.

After deformation, the midplane position is

$$\boldsymbol{R}(\zeta^\alpha) = \boldsymbol{r}(\zeta^\alpha) + \boldsymbol{v}(\zeta^\alpha). \tag{4}$$

Uppercase letters are used to denote shell variables associated with the deformed midplane and we now define: the deformed midplane base vectors, $\boldsymbol{A}_\alpha = \boldsymbol{R}_{,\alpha}$; deformed covariant midplane metric tensor, $A_{\alpha\beta} = \boldsymbol{A}_\alpha \cdot \boldsymbol{A}_\beta$, with determinant A; and deformed curvature tensor, $B_{\alpha\beta} = \boldsymbol{N} \cdot \boldsymbol{A}_{\alpha,\beta}$, where $\boldsymbol{N} = \boldsymbol{A}_1 \times \boldsymbol{A}_2/|\boldsymbol{A}_1 \times \boldsymbol{A}_2|$ is the unit normal to the deformed midplane.

The deformation of the midplane may be characterized by the strain and bending tensors, $\gamma_{\alpha\beta}$ and $\kappa_{\alpha\beta}$, respectively

$$\gamma_{\alpha\beta} = \tfrac{1}{2}(A_{\alpha\beta} - a_{\alpha\beta}), \quad \kappa_{\alpha\beta} = -(B_{\alpha\beta} - b_{\alpha\beta}).$$

The large bending deformations of the thin-walled elastic tube that occur in the present system only generate small strains, allowing us to employ a linear constitutive equation (Hooke's law). The principle of virtual displacements, which describes the shell's deformation, is then

$$\int_0^{2\pi}\int_{-\infty}^{\infty} E^{\alpha\beta\gamma\delta}\left(\gamma_{\alpha\beta}\delta\gamma_{\gamma\delta} + \frac{1}{12}\left(\frac{h}{R}\right)^2 \kappa_{\alpha\beta}\delta\kappa_{\gamma\delta}\right)\sqrt{a}\,\mathrm{d}\zeta^1\,\mathrm{d}\zeta^2 = \frac{1}{12}\left(\frac{h}{R}\right)^3 \frac{1}{1-\nu^2}\int_0^{2\pi}\int_{-\infty}^{\infty}\left(\frac{R}{h}\right)\boldsymbol{f}\cdot\delta\boldsymbol{R}\sqrt{A}\,\mathrm{d}\zeta^1\,\mathrm{d}\zeta^2. \tag{5}$$

$\boldsymbol{f} = \boldsymbol{f}^*/K$ is the traction per unit area of the deformed midplane, non-dimensionalized by the bending modulus of the shell, $K = E(h/R)^3/12(1-\nu^2)$ and $E^{\alpha\beta\gamma\delta}$ is the plane stress stiffness tensor, non-dimensionalized by Young's modulus

$$E^{\alpha\beta\gamma\delta} = \frac{1}{2(1+\nu)}\left(a^{\alpha\gamma}a^{\beta\delta} + a^{\alpha\delta}a^{\beta\gamma} + \frac{2\nu}{1-\nu}\,a^{\alpha\beta}a^{\gamma\delta}\right), \tag{6}$$

where $a^{\alpha\beta}$ is the contravariant metric tensor of the undeformed midplane. Appendix A illustrates the behaviour of such thin-walled elastic tubes when loaded by uniform external pressures.

2.3. *Boundary conditions*

2.3.1. *Fluid–solid coupling*

The no-slip boundary condition implies that the fluid velocity on the tube wall must be the same as the local wall velocity, and in the moving frame of reference

$$\boldsymbol{u} = \frac{\partial \boldsymbol{R}(\zeta^\alpha)}{\partial \zeta^1} \quad \text{on the tube walls.} \tag{7}$$

The fluid exerts a traction on the shell, and the load terms in the solid equation (5) are given by

$$f_i = P^{(\mathrm{ext})} N_i - \sigma Ca \left(pN_i - \left(\frac{\partial u_i}{\partial x_j} + \frac{\partial u_j}{\partial x_i} \right) N_j \right), \tag{8}$$

where $\boldsymbol{N}$ is the (inward) normal to the deformed shell midplane, $P^{(\mathrm{ext})} = P^{(\mathrm{ext})*}/K$ is the external pressure and $\sigma = \sigma^*/(RK)$ is the dimensionless surface tension, which represents the ratio of surface-tension forces to the tube's bending stiffness.

2.3.2. *'End' conditions*

As $\zeta^1 \to -\infty$ (far ahead of the bubble tip), the fluid is at rest and the (dimensionless) cross-sectional area of the tube is $A^*_\infty/R^2 = 4A_\infty$. We truncate the computational domain at $\zeta^1 = \zeta_s$ and assume that at this point the wall slope has become so small that a long-wavelength approximation applies (lubrication theory). Hence, the fluid equations reduce to a two-dimensional Poisson equation in the final cross-section:

$$\frac{\partial}{\partial x_\beta} \left(\frac{\partial u_3}{\partial x_\beta} \right) = G \quad \text{at } \zeta^1 = \zeta_s, \tag{9a}$$

subject to the no-slip boundary condition

$$u_3 = \frac{\partial \boldsymbol{R}}{\partial \zeta^1} \cdot \boldsymbol{e}_3 \quad \text{on the tube wall.} \tag{9b}$$

Here, $\beta = 1, 2$ (the transverse directions) and $\boldsymbol{e}_3$ is the unit vector in the x_3-direction. G is a constant pressure gradient that must be determined as part of the solution. The solution of equations (9*a, b*) is applied as a Dirichlet boundary condition for the axial velocity component, u_3, and traction-free boundary conditions are applied for the transverse velocities. In the moving frame, the fluid has uniform unit velocity as $\zeta^1 \to -\infty$ and hence the axial flow rate in any cross-section must equal $4A_\infty$. This constraint is used as an additional equation to determine the extra variable G:

$$\int\int u_3|_{\zeta^1 = \zeta_S} \, \mathrm{d}x_1 \, \mathrm{d}x_2 = 4A_\infty. \tag{9c}$$

Far behind the bubble tip, we truncate the domain at $\zeta^1 = \zeta_F$, set $u_3 = 1$ and apply traction-free boundary conditions in the other coordinate directions, allowing the development of transverse draining flows. At both ends of the domain, instead of matching to the decaying eigenfunctions explicitly, the axial gradients of the transverse wall displacements are set to zero. On doubling the length of the domain the results were found to change by less than 0.5%, indicating that this approximation is suitably accurate. Finally, rigid body motions are suppressed by setting the axial wall displacement to zero at $\zeta^1 = \zeta_F$, far behind the bubble tip.

2.4. *Numerical implementation*

The coupled system of equations (1*a, b*), (2*a–c*), (5), (7), (8), (9*a–c*) was solved numerically using a finite-element method. The method of solution in the fluid

domain is exactly the same as that described by Hazel & Heil (2002). Briefly, the fluid domain, shown in figure 2, is decomposed into N_F three-dimensional, Taylor–Hood finite elements (Taylor & Hood 1973) and the nodal positions of the fluid mesh near the free surface are adjusted by the method of spines (Kistler & Scriven 1983). The solid domain is decomposed into N_S two-dimensional Hermite finite elements (Bogner, Fox & Schmit 1967). We impose symmetry at the planes $x_1 = 0$ and $x_2 = 0$, which permits the restriction of the computational domain to positive values of the transverse coordinates, $x_1 \geqslant 0$, $x_2 \geqslant 0$ and $\zeta^2 \in [0, \pi/2]$.

An automatic mesh generation scheme deforms the fluid mesh in response to changes in the position of the wall and the air–liquid interface. For this purpose an initial mesh is generated in the undeformed tube. The position of each fluid node is then represented as a function of the Lagrangian surface coordinates, ζ^α, using a generalized spine method. After deformation, the positions of the nodal points are recalculated based upon the new positions of the material points on the wall. The mesh thus deforms with the tube, see figure 2.

The weak form of the Stokes equations (C 1*a–c*) and the variational equations for the shell (C 2), both shown in Appendix C, were discretized and solved simultaneously by a Newton–Raphson method. A frontal scheme (Duff & Scott 1996) was used to assemble the Jacobian matrices and solve the resulting linear systems.

For a typical initial guess, the residuals are of $O(1)$ and the Newton iteration was deemed to have converged when the absolute value of the largest residual is less than 10^{-8}. The initial guess was generated by using Hazel & Heil's (2002) code to find the flow field corresponding to a bubble propagating through a rigid circular tube at low Ca ($Ca = 0.5$). The flow rate from the rigid-tube computation was then used as the initial value of A_∞ in a computation with weak fluid–structure interaction ($\sigma = 0.001$). From this initial guess, a converged solution of the fully coupled system was obtained in 7–8 Newton steps. A continuation technique was then used to step through different values of Ca, σ and A_∞. At the standard resolution of 43 000 degrees of freedom, one Newton iteration requires about fifteen minutes of CPU time on a 1.4 GHz Linux PC.

The fluid solver has been previously validated in problems of bubble propagation in rigid tubes (Hazel & Heil 2002). The newly developed shell solver was validated by comparison with an existing shell solver used previously by Heil (1997). Further validations included a comparison of the computed buckling loads with theoretical predictions (Yamaki 1984) and a comparison of the non-axisymmetric tube shapes under uniform pressure loading with the predictions from Flaherty, Keller & Rubinow (1972) inextensible Euler–Bernoulli model.

The spatial convergence of the results was assessed by repeating selected studies with higher spatial resolution, see figure 10. Finally, the effect of varying the length of the computational domain was investigated. The standard length was 40 dimensionless units ($-20 \leqslant x_3 \leqslant 20$) and the results were found to change by less than 0.5% on doubling the domain length to 80 ($-40 \leqslant x_3 \leqslant 40$), see figures 3 and 5(*a*).

3. Results

Throughout this work, we used a Poisson's ratio of $\nu = 0.49$ to reflect the near incompressibility of lung tissue. The wall thickness was set to $h/R = 1/20$, close to the upper limit of applicability of thin-shell theory. The external pressure is taken to be the reference pressure and was set to zero, $P^{(\mathrm{ext})} = 0$. The non-dimensional surface tension, σ, represents the ratio of surface-tension forces to the bending stiffness of

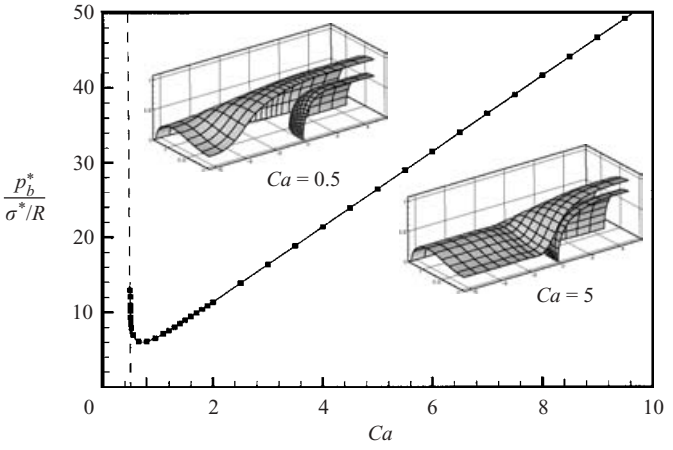

FIGURE 3. Bubble pressure vs. capillary number for the standard system parameters (solid line). The symbols show the results obtained from a calculation in which the length of the computational domain was doubled. The dashed line is the asymptotic prediction for the behaviour on the 'pushing' branch, see § 3.1.1(*a*). Inset figures illustrate tube and interface shapes on the two branches.

the tube and unless otherwise stated we used $\sigma = 1$. The standard value for the cross-sectional area of the buckled end of the tube was set to $A_\infty = 0.373$, which corresponds to maximum inward radial displacement of 80% of the tube's undeformed radius. (Recall that $A_\infty = A_\infty^*/(4R^2)$ and so for an undeformed axisymmetric tube $A_\infty = \pi/4 \approx 0.785$.)

3.1. *Variations in bubble speed: Ca*

3.1.1. *Bubble pressure*

Figure 3 shows the bubble pressure on the capillary scale as a function of the propagation speed, expressed in dimensionless form by the capillary number. Qualitatively, the behaviour is similar to that predicted by the two-dimensional models.

(*a*) *Low capillary number – the 'pushing' branch*

At low values of the capillary number, the slope of the p_b–Ca curve is negative and a decrease in bubble pressure is required to increase the propagation speed. Examination of the fluid domain reveals that, as in the two-dimensional model, a large volume of fluid is being pushed ahead of the air finger. Furthermore, the air finger is located in a region in which the tube is uniformly inflated. This observation motivates the development of a simple model for the system's behaviour in this regime.

The air finger is moving in a region of nearly constant tube shape and so we expect its behaviour to be similar to that of a finger propagating into a rigid circular tube of the same radius. In that system, Bretherton (1961) and many others have shown that the thickness of the deposited film divided by the tube radius, h_∞/R_T, decreases with Ca, eventually approaching zero as $Ca \to 0$ and a static hemispherical bubble fills the entire tube. In the present problem, conservation of mass demands that the cross-sectional area occupied by the fluid at the open end of the tube must equal that

at the closed end, from which we derive

$$R_T^2 = \frac{4A_\infty}{\pi(h_\infty/R_T)\,(2-(h_\infty/R_T))}. \tag{10}$$

Given that $h_\infty/R_T \to 0$ as $Ca \to 0$, this implies that the open end of the tube must inflate dramatically as the capillary number decreases. This inflation can only be achieved by a large increase in internal bubble pressure and hence, at low Ca, $p_b^*/(\sigma^*/R)$ must increase as Ca decreases.

Numerical results for h_∞/R_T, as a function of Ca, in an axisymmetric rigid tube are shown in Appendix B. Inserting these results into equation (10) yields $R_T(Ca)$. Finally, using the pressure–radius relationship for a uniformly inflated tube, given in Appendix A, we obtain an expression for the bubble pressure as a function of the capillary number, $p_b(Ca)$. The predictions of this model agree well with the computational results at low Ca, see figure 3.

Gaver *et al.* (1996) presented a similar analysis for the two-dimensional problem with equally good agreement between the model predictions and computational results. The behaviour at small Ca is a consequence only of the facts that (i) mass is conserved and (ii) $h_\infty/R_T \to 0$, as $Ca \to 0$. Statements (i) and (ii) are true in both two and three dimensions, which explains why both models exhibit the qualitatively similar two-branch behaviour. Horsburgh (2000) showed that, for pressure-driven flows, the 'pushing' branch is unstable in the two-dimensional model and we presume that this is also the case in three dimensions.

(*b*) *High capillary number – the 'peeling' branch*

At high Ca, an increase in bubble pressure causes an increase in propagation speed, which is the physically expected behaviour. Figure 3 shows that on the 'peeling' branch, $p_b^*/(\sigma^*/R) \propto Ca$ and a linear regression analysis for $1 \leqslant Ca \leqslant 10$ shows that $p_b^*/(\sigma^*/R) \approx 1.43 + 5.02\,Ca$, with a correlation coefficient $r^2 = 0.999$. Thus, for large Ca the bubble pressure is approximately constant on the viscous scale, $p_b^*/(\mu U/R) \approx 1.43/Ca + 5.02$.

The explanation for this behaviour is that the tube approaches a limiting geometrical configuration as Ca increases: ahead of the bubble tip, the tube has the cross-section specified by A_∞ and the tube is held in this configuration by the negative fluid pressure $p = -\mathscr{P}_{\mathrm{tm}}(A_\infty)$, see Appendix A. The tube is reopened by the rise in fluid pressure in the vicinity of the bubble tip; behind the bubble tip, the fluid pressure rapidly approaches another constant value which maintains the tube in its distended state. The pressure rise experienced by the wall increases with Ca, equation (8), but once the reopened section of the tube has become inflated it becomes very stiff and so even relatively large changes in internal pressure do not significantly affect the wall shape behind the tip.

The air finger also approaches a limiting shape as Ca increases. This is similar to the behaviour observed during the propagation of air fingers into rigid tubes (e.g. Cox 1962 and Appendix B). Hence, the shape of the entire fluid domain and with it the flow field and stresses (on the viscous scale) become independent of Ca.

3.1.2. *Flow fields*

Figure 4 illustrates the tube shapes, fluid pressures and streamlines over a range of capillary numbers. At the lowest values of Ca, the system is on the 'pushing' branch and the tube remains inflated for some distance ahead of the bubble tip. In two dimensions, a closed vortex develops ahead of the bubble tip in this mode,

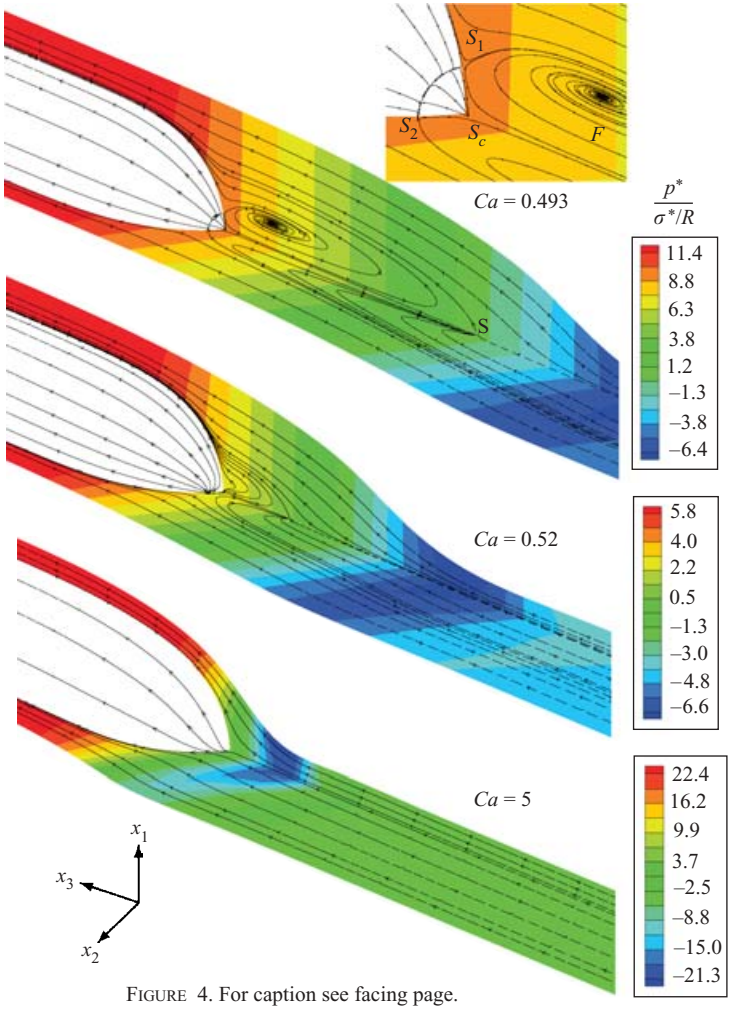

FIGURE 4. For caption see facing page.

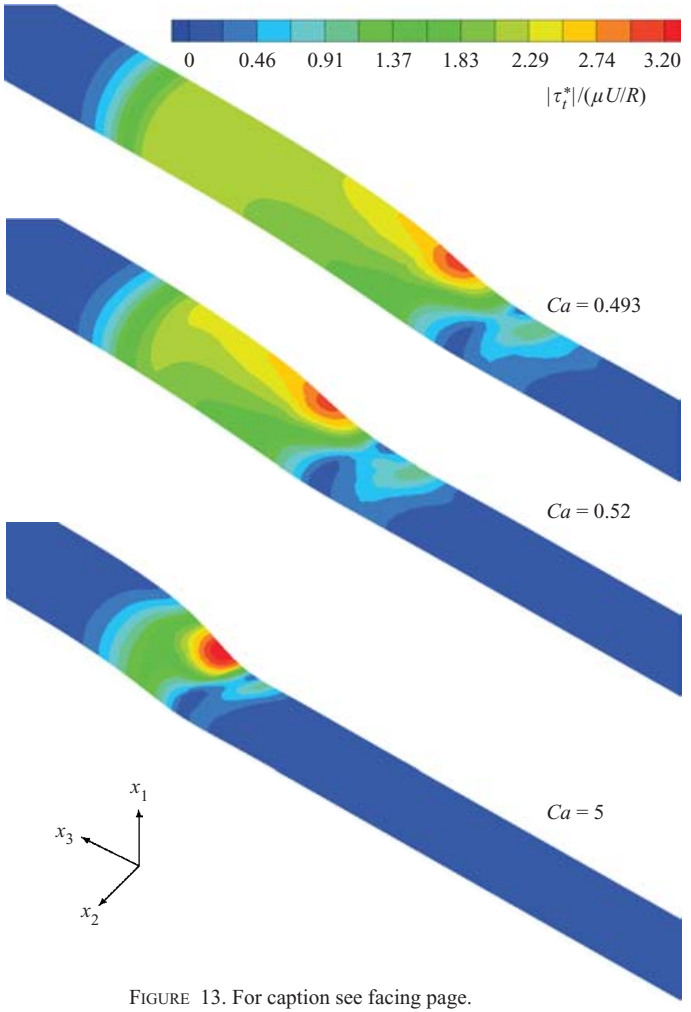

FIGURE 13. For caption see facing page.

see figure 1. In three dimensions, there are no closed vortices; instead, a horseshoe vortex forms ahead of the tip, emanating from the two-dimensional focus in the plane $x_2 = 0$, marked F in figure 4. As Ca increases, the focus moves towards the bubble where it merges with the saddle point S_1 on the bubble in the plane $x_2 = 0$. The horseshoe vortex disappears, although a small reversed-flow region remains ahead of the tip. Further increasing Ca causes the remaining reversed-flow region to disappear when the stagnation point ahead of the bubble tip, S, reaches the tip and merges with S_c. Ultimately, the stagnation points S_2 and S_c merge, leaving only S_c at the tip: complete bypass flow. The transport properties of the flow in three dimensions are therefore quite different to those of the two-dimensional models. In particular, the bulk transport of any surfactant in the system, and the consequent effects upon the overall dynamics, could be greatly influenced by the lack of a closed vortex in three dimensions.

Increasing Ca causes the buckled region of the tube to move closer to the bubble tip and a 'neck' develops, where the local cross-sectional area of the tube is less than A_∞. The 'neck' is the site of the greatest negative fluid pressure, which pulls the wall inwards. A similar effect has been observed in the two-dimensional models (Gaver *et al.* 1996; Heil 2000). Gaver *et al.* (1996) and Heil (2001) showed that the 'neck' is caused by damped oscillatory eigensolutions for the wall displacement field far ahead of the bubble tip. The contours in figure 4 also demonstrate that the fluid pressure is approximately constant in each cross-section, apart from the 'neck' region where a noticeable transverse pressure gradient develops.

3.1.3. *Finger shapes*

Figure 5(*a*) shows the radii of the air finger taken in the horizontal and vertical planes of symmetry, r_1 and r_2, respectively, at $x_3 = 15$. At low Ca, on the 'pushing' branch, the air finger is axisymmetric and both radii have the same value. As Ca increases, however, the radii begin to differ and at $Ca = 5$, the finger is noticeably non-axisymmetric at this point, as shown in figure 5(*b*). This asymmetry is caused by the mechanism identified by Hazel & Heil (2002) in their study of bubble propagation in rigid, non-circular tubes. In such tubes, the non-axisymmetric passage of fluid around the tip of the bubble necessitates a non-uniform transverse pressure distribution which causes the air–liquid interface to become locally non-axisymmetric, even if it ultimately approaches an axisymmetric shape far behind the tip. Hazel & Heil (2002) found that this effect becomes more pronounced as Ca increases because longer axial distances are required for the relatively weak surface tension forces to return the interface to an axisymmetric shape. In elastic tubes, the effect is enhanced by additional transverse flows caused by the sidewalls moving inwards as the tube reopens. At high Ca, therefore, even if the tube becomes approximately axisymmetric a short distance behind the bubble tip, the interface remains visibly non-axisymmetric for much longer distances downstream.

FIGURE 4. Streamlines in the planes $x_1 = 0$, $x_2 = 0$ and on the surface of the air finger, for $A_\infty = 0.373, \sigma = 1$. Contours of fluid pressure on the capillary scale, $p^*/(\sigma^*/R)$ are also presented.

Figure 13. Contours of the magnitude of the tangential component of the wall shear stress, $|\tau_t|$, for $A_\infty = 0.373$, $\sigma = 1$ and $Ca = 0.493, 0.52, 5$. The shear stress is presented on the viscous scale.

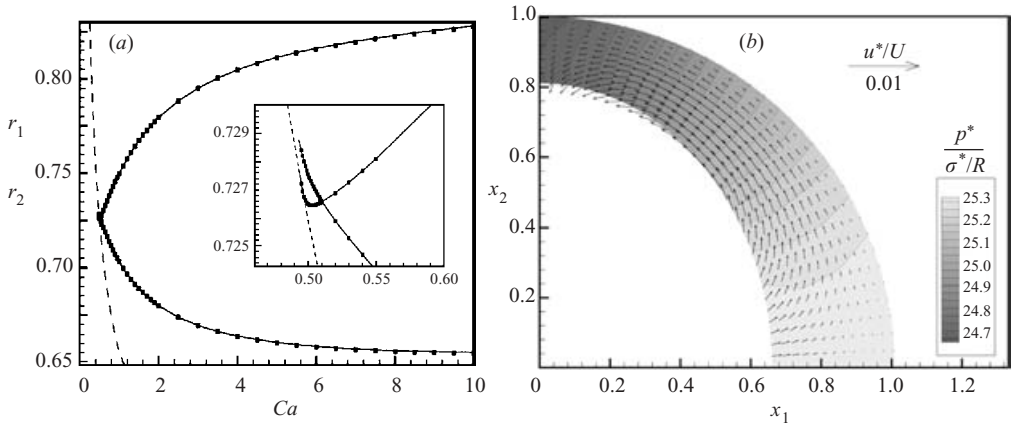

FIGURE 5. (*a*) Bubble radii vs. capillary number at $x_3 = 15$. r_1 is the radius in the x_1-direction, in the plane $x_2 = 0$ and r_2 is the radius in x_2-direction, in the plane $x_1 = 0$. The dashed line shows the 'pushing' model's (§3.1.1*a*) prediction of the axisymmetric bubble radius. The symbols are the results obtained from a computation in a longer domain. The inset graph is an enlargement of the low-Ca region. (*b*) Cross-section at $x_3 = 15$ for $Ca = 5$ demonstrating the non-axisymmetric bubble interface, transverse pressure gradient and persisting draining flows.

3.2. *Parameter variations*

For bubble propagation in rigid tubes, Bretherton (1961) and many others have demonstrated that the ultimate finger radius is set by the interaction between viscous and surface-tension effects near the finger tip, at least at small Ca. In the present problem, the deformability of the tube adds a further level of complexity to this interaction. Once the finger radius has been determined, however, the tube shape far behind the tip follows directly from mass conservation and the bubble pressure adjusts to ensure that the required tube shape is realized. The consequences of this behaviour are explored in the following parameter studies.

3.2.1. *Variations in the degree of collapse: A_∞*

Figure 6 shows the bubble pressure as a function of the capillary number for three different values of A_∞. The bubble pressure required to drive the air finger at a given speed decreases with decreasing A_∞: it is easier to reopen a more strongly buckled tube. This somewhat counter-intuitive result may be understood by remembering that, in the present problem, the fluid far ahead of the bubble is at rest. (A brief discussion of the difference between this boundary condition and that appropriate to bubble propagation in rigid tubes (Bretherton 1961) is given in Appendix D.) The propagating bubble redistributes the fluid from the occluding plug into a thin film. Thus, the larger the cross-sectional area ahead of the air finger, the greater the work required in redistribution and the higher the pressure required to drive the flow. In addition, as A_∞ increases, the transmural pressure (external minus internal pressure), $\mathscr{P}^*_{\rm tm}$, far ahead of the bubble must decrease (see figure 14), which requires an increase in the fluid pressure because $P^{(\rm ext)} = 0$. This effect provides only a small contribution to the differences in bubble pressures in figure 6, however. For instance, on the peeling branch $p^*_b(A_\infty = 0.45) - p^*_b(A_\infty = 0.373) \approx 10\sigma^*/R$, whereas the difference in transmural pressures far ahead of the bubble tip is $\mathscr{P}^*_{\rm tm}(A_\infty = 0.45) - \mathscr{P}^*_{\rm tm}(A_\infty = 0.373) \approx 0.3\sigma^*/R$, see Appendix A and recall that $\sigma = \sigma^*/RK = 1$ in figure 6.

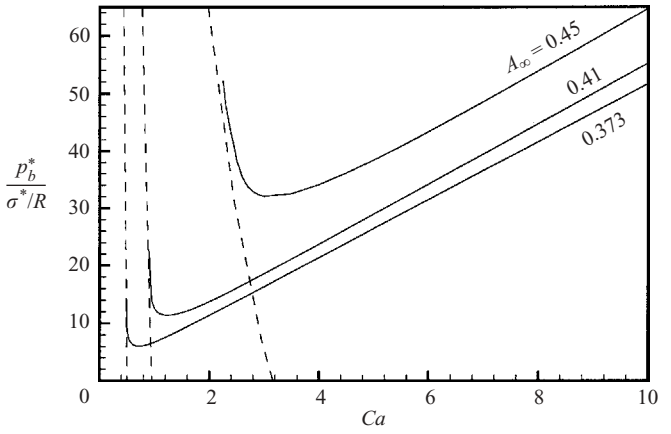

FIGURE 6. Bubble pressure vs. capillary number for $\sigma = 1$ and $A_\infty = 0.373, 0.41, 0.45$. The dashed lines are the asymptotic predictions based upon § 3.1.1(*a*).

Figure 6 also shows that, as the degree of tube collapse decreases, not only are higher pressures required to initiate steady bubble motion, but such motion only exists at higher propagation velocities. This phenomenon may be understood from the 'pushing' model, § 3.1.1(*a*), which also predicts this behaviour. In rigid tubes, the cross-sectional area occupied by the fluid film far behind the bubble tip increases with capillary number, see Appendix B. Hence, if the system is in the 'pushing' mode, as A_∞ increases, the capillary number at which the (elastic) tube must first become inflated in order to conserve mass increases and the p_b–Ca curve shifts to the right, as observed.

At the largest area, $A_\infty = 0.45$, the prediction from the 'pushing' model, § 3.1.1(*a*), begins to deviate from the numerical results. This is because for this value of A_∞ the 'pushing' branch develops at $Ca \approx 3$. At this relatively large capillary number the tip asymmetry, referred to in § 3.1.3, causes the air–liquid interface to remain non-axisymmetric for significant distances behind the bubble tip. This deviation from the axisymmetric geometry assumed in the 'pushing' model is sufficient to cause the observed disagreement between the model and numerical results.

Figure 7 shows the results for the bubble pressure plotted against A_∞ for various capillary numbers. As A_∞ increases, the increase in cross-sectional area occupied by the fluid at the open end of the tube must be effected by a decrease in the radius of the air finger and/or an increase in the radius of the wall. Examination of the fluid domains, shown in figure 8, indicates that at low values of A_∞, the additional fluid is initially accommodated by a decrease in bubble radius without a noticeable change in wall shape or bubble pressure. At each Ca, however, there is a critical value of A_∞ above which the bubble radius no longer decreases and the open end of the tube must inflate axisymmetrically to ensure conservation of mass of the fluid. The elastic tube is very stiff under inflation and hence the bubble pressure must then rise very steeply as seen in figure 7. For $Ca = 1$, the system is in the 'pushing' mode at this point, see figure 6, and the 'pushing' model, § 3.1.1(*a*), agrees well with the numerical predictions. At higher Ca, the tube is in the 'peeling' mode when the tube begins to inflate and the 'pushing' model does not apply. Nonetheless, at every Ca, it is expected that the solution will eventually match onto the 'pushing' model, once A_∞ is high enough, because the 'pushing' branch shifts to higher Ca as A_∞ increases, see

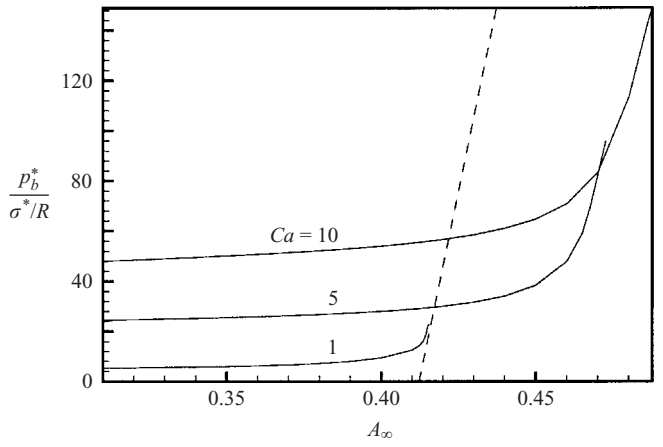

FIGURE 7. Bubble pressure vs. A_∞ for $\sigma = 1$. The dashed line is the prediction based upon the 'pushing' model, § 3.1.1(*a*), for $Ca = 1$.

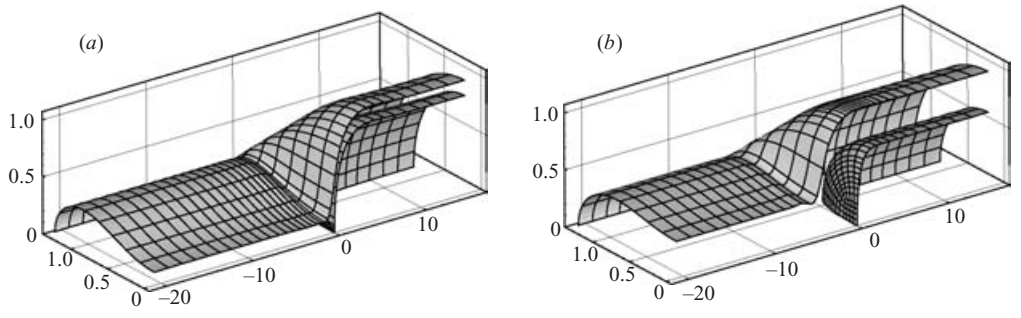

FIGURE 8. Interface and tube shapes for $Ca = 5$, $\sigma = 1$ and (*a*) $A_\infty = 0.31$, (*b*) $A_\infty = 0.47$.

figure 6. Additionally, once $A_\infty > \pi/4$ the tube is axisymmetrically inflated ahead of the bubble tip and must be further inflated behind the tip in order to accommodate the air finger. Hence, at large A_∞, the system is completely axisymmetric, satisfying the assumptions underlying the derivation of the 'pushing' model in § 3.1.1(*a*).

3.2.2. *Variations in the dimensionless surface tension: σ*

An increase in the non-dimensional surface tension, $\sigma = \sigma^*/RK$, can be caused either by an increase in physical surface tension, σ^*, or by a reduction in wall stiffness, K. The load on the wall is proportional to the product of σ and the capillary number, see equation (8). In terms of the wall mechanics, therefore, the effect of an increase in σ is similar to the effect of increasing Ca: the pressure jump experienced by the wall, near the bubble tip, increases. The increase in pressure behind the bubble tip causes the tube there to become more inflated, and the increase in magnitude of the pressure jump causes the reopening to take place over shorter axial lengthscales, see figure 9. As σ increases and the tube becomes more inflated the interface curvature actually decreases, leading to a slight decrease in the capillary pressure drop over the bubble tip. Nevertheless, the pressure jump experienced by the wall increases because although κ itself decreases, the load on the wall is given by the product $\sigma\kappa$.

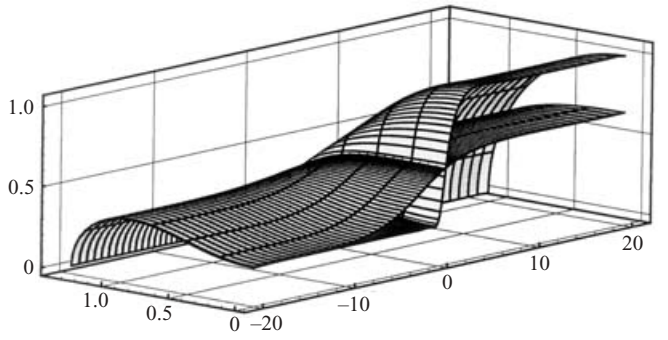

FIGURE 9. Tube shapes for $\sigma = 0.002$ and 1. In both cases $Ca = 10$ and the tubes have the same cross-sectional area, $A_\infty = 0.373$, at the buckled end. The reopening region and tube shapes at the open end are very different, however. In particular, the tube is still buckled at the open end when $\sigma = 0.002$.

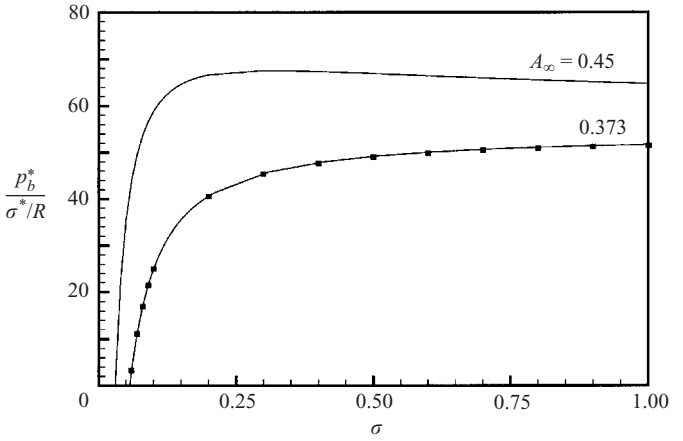

FIGURE 10. Bubble pressure vs. σ for a fixed value of $Ca = 10$ and $A_\infty = 0.373, 0.45$. The symbols show the results computed on the same domain using a refined mesh.

At sufficiently high values of σ, the tube approaches a limiting geometrical configuration: that which occurs if a large step change in pressure is applied at the bubble tip. Once such a configuration has been attained, the system becomes virtually independent of σ. This effect is demonstrated in figure 10, which shows the bubble pressure plotted against σ at a fixed capillary number, $Ca = 10$, for $A_\infty = 0.373$ and 0.45.

Figure 11 demonstrates the effects of varying the non-dimensional surface tension, σ, upon the p_b–Ca relationship. The pressure and velocity scales both involve σ^* and, hence, the variations in $\sigma = \sigma^*/(RK)$ should be interpreted as changes in the tube's bending stiffness, K.

For $A_\infty = 0.373$, an increase in tube stiffness causes a monotonic decrease in bubble pressure, at any given Ca. At the lowest value of σ shown ($\sigma = 0.1$), the bubble pressure is negative at low values of Ca, which indicates that the tube is still buckled at the open end. It is therefore possible to have steadily propagating bubbles in tubes that remain buckled provided that σ is small. An example of such a configuration is shown in figure 9.

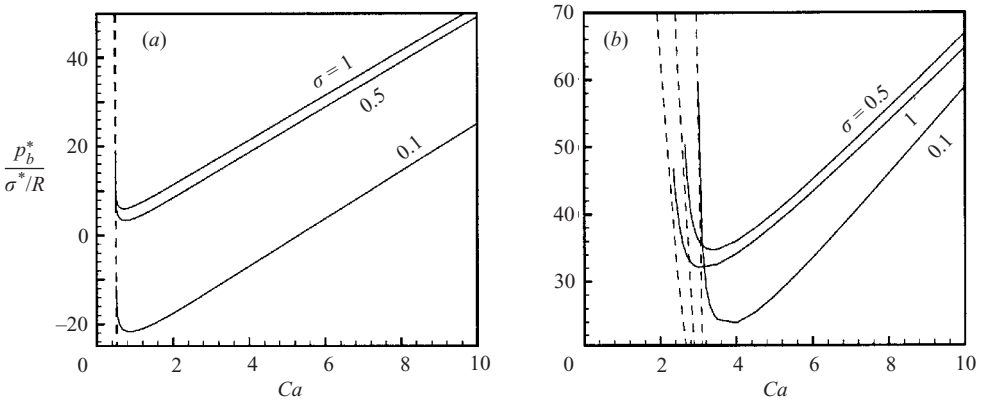

FIGURE 11. Bubble pressure vs. capillary number for $\sigma = 0.1, 0.5, 1$ and (*a*) $A_\infty = 0.373$, (*b*) 0.45. The dashed lines are predictions from the 'pushing' model, § 3.1.1(*a*).

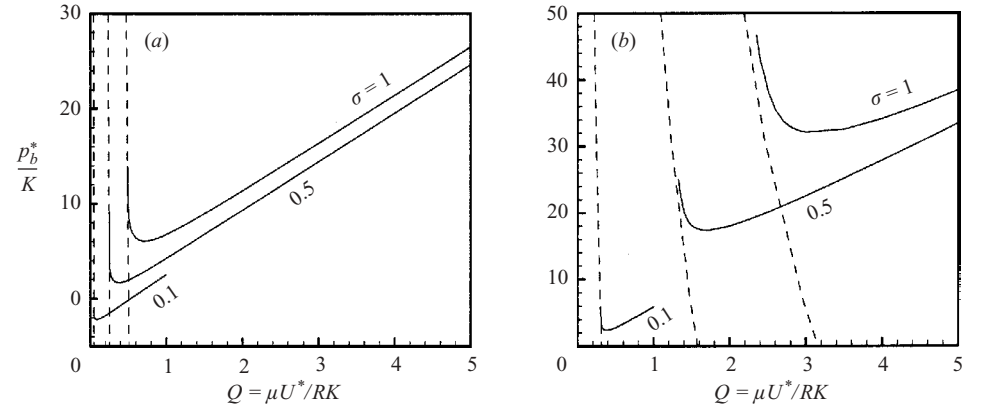

FIGURE 12. Bubble pressure vs. capillary number for $\sigma = 0.1, 0.5$ and 1 and (*a*) $A_\infty = 0.373$, (*b*) 0.45. The dashed lines are results from the 'pushing' model, § 3.1.1(*a*). The data are the same as those shown in figure 11, but they are here presented on a surface-tension-independent scale.

For $A_\infty = 0.45$, the change in bubble pressure with tube stiffness is not monotonic and the curve for $\sigma = 0.5$ lies above that for $\sigma = 1$. This behaviour is caused by the presence of a local maximum in the $p_b(\sigma)$ curve, as seen in figure 10 for $A_\infty = 0.45$ and $Ca = 10$. In fact, local maxima appear to be generic features of $p_b(\sigma)$ curves at constant Ca. For sufficiently large σ, as σ continues to increase the only changes in the fluid domain are a (slight) inflation of the tube behind the bubble tip and a (slight) decrease in the distance between the bubble tip and the tube wall. These changes cause a decrease in the volume of the region of significant fluid motion and hence a decrease in the fluid dissipation, leading to the observed (small) decrease in bubble pressure, on the viscous scale, as σ increases yet further.

Figure 12 shows the same data on a surface-tension-independent scale. The pressure is non-dimensionalized by the tube's bending stiffness and the bubble speed is expressed as $Q = \sigma Ca = \mu U/(RK)$, which represents the ratio of viscous forces to the bending stiffness of the tube.

The figure shows that, at a given bubble speed, an increase in physical surface tension, σ^*, causes an increase in bubble pressure. A higher value of σ^* also leads to an increase in $p^*_{\min}$ and an increase in the propagation speed at $p^*_b = p^*_{\min}$. For $A_\infty = 0.45$, the approximation from the 'pushing' model, § 3.1.1(*a*) loses accuracy at higher values of σ. This is again a consequence of the tip asymmetry, § 3.1.3, the effect of which becomes even more pronounced at higher σ because the loading on the tube wall increases linearly with σ, see equation (8).

3.3. *Fluid traction on the airway wall*

In the context of airway reopening it is important to assess the stresses that the fluid exerts on the wall as it is vital to avoid damage to the lung tissue.

Figure 13 shows the magnitudes of the tangential component of the wall shear stress, τ_t. Far from the bubble tip, the stress tends to zero because the fluid is at rest. The maximum tangential shear stress is exerted at the point of greatest axial wall slope and increases with *Ca*. The maximum shear was also found to increase with an increase in σ or a decrease in A_∞. These effects are a result of the changes in the geometry of the reopening region under parameter variations and the maximum shear stress increases with increasing wall slope. The changes are all relatively minor, however, and, on the viscous scale, the maximum tangential shear stress varies in the range $2 < \tau^*_t/(\mu U/R) < 5$ for all the parameter regimes investigated in this paper.

The normal stress is dominated by the contribution of the pressure, see figure 4, and is, in general, greater than the tangential shear stress shown in figure 13. We further find that the normal stresses on the wall do not vary greatly with azimuthal position and are smallest in the buckled region and greatest in the region occupied by the bubble. Finally, we observe that axial gradients in both the normal and tangential components of the fluid traction increase with increasing wall slope, see figures 4 and 13.

4. Discussion

In this paper we have developed a fully consistent model of bubble propagation in three-dimensional elastic tubes. The free-surface Stokes equations are coupled to the equations of geometrically nonlinear shell theory and were solved numerically over a wide range of system parameters.

A generic two-branch behaviour of the p_b–*Ca* relationship was found, qualitatively confirming the results of previous two-dimensional models (Gaver *et al.* 1996). The low-*Ca* 'pushing' branch is a direct consequence of mass conservation and the fact that the ratio of the trailing film thickness to the tube radius behind a moving air finger in an axisymmetric tube tends to zero with *Ca*. This mechanism is independent of the spatial dimension of the system and hence is observed in both two- and three-dimensional models. At sufficiently high σ and *Ca*, the tube shape becomes approximately constant, tending towards the limiting shape that would occur if a large step change in pressure were imposed at the bubble tip. The tube shape ahead of the bubble will be of the specified cross-sectional area, A_∞, and behind the bubble the tube will be inflated. Elastic tubes become very stiff under inflation and hence even large further increases in the internal pressure will not cause significant changes in the tube shape. The pressure drop on the viscous scale, therefore, tends to a constant as *Ca* increases and $p^*_b/(\sigma^*/R) \propto Ca$ on the high-*Ca* 'peeling' branch. This behaviour has not been observed in Gaver *et al.*'s (1996) two-dimensional model, where neither the membrane nor the linear springs stiffen under inflation and hence

the wall shape continues to change significantly under increasing *Ca*. In principle, it would be possible to modify the two-dimensional model to capture this aspect of the three-dimensional system by using suitable nonlinear springs.

An important consequence of the two-branch behaviour is the existence of a minimum bubble pressure, $p^*_{\min}$, below which there are no steady solutions. Gaver *et al.* (1996) have already noted that $p^*_{\min}$ is an upper bound for the experimentally observed yield pressure. There could well be a range of pressures below $p^*_{\min}$ for which the bubble starts to move, but never reaches a steadily propagating state. If such transient motion of the bubble is sufficient to clear the (finite) blockages in the lung, then a steady state may never be achieved, or indeed required, in ventilation applications. Nevertheless, the trends affecting $p^*_{\min}$ would still be expected to apply to the yield pressure.

We have shown that Gaver *et al.*'s (1996) two-dimensional model successfully predicts (albeit qualitatively) many features of three-dimensional airway reopening. Features that are not captured by the two-dimensional model include the observation that an increase in the cross-sectional area of the tube far ahead of the bubble causes an increase in bubble pressure. Higher pressures are therefore required to reopen less strongly buckled tubes because a greater volume of fluid must be redistributed per unit time. An increase in the volume of liquid lining the lung, e.g. caused by asthma or pulmonary œdema, would therefore appear to be extremely dangerous. Not only will the thicker film be more susceptible to the Rayleigh instability, which initially causes the airway to collapse (Halpern & Grotberg 1992), but once in the buckled state, the large volume of fluid will make the airway more difficult to reopen.

Another important difference between the two- and three-dimensional models is the change in the flow fields ahead of the bubble tip. At low values of the capillary number, in the frame of reference moving with the bubble, a closed vortex develops ahead of the tip in two dimensions. In contrast, an open horseshoe vortex is formed in three dimensions. These differences in the bulk transport properties of the fluid could lead to significant changes in the effects of surfactant upon the three-dimensional system compared to previous observations. For example, Ghadiali *et al.* (2001) studied the propagation of a bubble into a rigid axisymmetric tube and found that at low surfactant concentrations, bulk transport to the interface was reduced at low *Ca*, leading to an increase in the interfacial pressure jump. It is unclear whether this effect will occur to the same extent in the three-dimensional system where surfactant cannot remain trapped in the vortex.

Variations in the dimensionless surface tension, $\sigma = \sigma^*/(RK)$, may be interpreted as changes in either the wall stiffness or the surface tension of the liquid lining the airways. At high values of σ, the wall slopes and the pressure on the viscous scale appear to become independent of σ. This is again a consequence of the tube approaching a constant shape – the limit of a very flexible tube. A decrease in wall stiffness or increase in surface tension (increase in σ) tends to cause an increase in bubble pressure and an increase in $p^*_{\min}$. (In some parameter regimes, $p_b(\sigma)$ can have a weak local maximum before p_b becomes approximately independent of σ on the capillary or viscous scales.) It follows that it would be expected to be harder to reopen the lungs of patients with respiratory distress syndrome, in which the surface tension is increased, or with diseases that cause a weakening of the airway walls.

In an attempt to restrict the number of parameters in our model and keep it as simple as possible, we have deliberately not included an elastic bedding, which could represent the effect of parenchymal tethering in the lung, or axial tension, which were both present in Gaver *et al.*'s (1996) model. Consequently, our model does not have

an equivalent to the parameter $\Gamma = K_{\text{spring}} H^2/\sigma^*$ defined by Gaver *et al.* (1996). Their parameter η, a dimensionless wall tension, plays a role loosely equivalent to σ^{-1} in that an increase in σ causes a shortening of the reopening region.

The greatest stresses exerted on the cells lining the airways are due to the fluid pressure. After passage of the air finger the airway wall can be subject to very large fluid pressures. It is therefore imperative that p_b^* be kept as low as possible during any therapeutic procedure. For any given parameter combination, p_{min}^* is an upper bound for the transmural pressure required to reopen the airway. In our model, $p_{\text{min}}^*/(\sigma^*/R)$ ranges from approximately -20 to 30 over the parameters variations presented. Negative values of p_{min}^* occur in situations in which the airway remains buckled (non-axisymmetric) after the passage of the air finger, and this indicates that the bubble pressure is lower than the external (pleural) pressure in the lung. Under these conditions, the reopening is driven by the elastic restoring force of the airway wall, as opposed to an applied positive bubble pressure.

The tangential component of the viscous wall shear stress, $\tau_t^*/(\mu U/R)$, is found to be largely insensitive to changes in the system parameters, with a maximum value between 2 and 5. In dimensional terms, the maximum tangential wall shear stress is $\tau_{t_{\text{max}}}^* = Ca(\sigma^*/R)\tau_{t_{\text{max}}}$ and so the capillary number must be kept as small as possible to minimize the shear stresses on the airway wall. In fact, steady reopening of the airway at $p_b^* \approx p_{\text{min}}^*$ will minimize both normal and shear stresses. Nonetheless, the maximum tangential wall shear stress can be extremely large. For example, consider the steady reopening of the bronchi in the tenth generation of the lung, assuming that $A_\infty = 0.373$ and that we can reopen at $p_b^* = p_{\text{min}}^*$. In such bronchi, $R \approx 0.06\,\text{cm}$, $h/R \approx 0.1$ and $E \approx 6 \times 10^4\,\text{dyn cm}^{-2}$ (Halpern & Grotberg 1992), giving $K \approx 0.66\,\text{N m}^{-2}$. The surface tension of the lung lining fluid is approximately that of water, $\sigma^* = 2.0 \times 10^{-2}\,\text{N m}^{-1}$ and so $\sigma = \sigma^*/(KR) \approx 50$. For these parameters, we find that $Ca \approx 0.29$ at $p_b^* = p_{\text{min}}^*$ and $\tau_{t_{\text{max}}} \approx 4$, which yields a maximum dimensional wall shear stress of $\tau_{t_{\text{max}}}^* \approx 40\,\text{N m}^{-2}$. In comparison, Fry (1968) found that a shear stress of $40\,\text{N m}^{-2}$ was sufficient to remove aortic endothelial cells from the arterial wall.

The above analysis is independent of the dimensional bubble propagation speed, $U = \sigma^* Ca/\mu$. If we assume the viscosity of the lung lining fluid to be that of water, $\mu \approx 10^{-3}\,\text{kg m}^{-1}\,\text{s}^{-1}$, then the propagation speed would be $U = \sigma^* Ca/\mu \approx 6\,\text{m s}^{-1}$, a completely unrealistic scenario. In that case, the airway reopening must be either (*a*) an intrinsically unsteady phenomenon, and/or (*b*) driven by volume rather than pressure control. In the latter case, the system could undergo steady reopening on the 'pushing' branch, leading to high bubble pressures, but lower shear stresses. Alternatively, mucus secretions (e.g. in asthma, cystic fibrosis and bronchitis) can lead to significant elevation of the viscosity of lung lining fluid. Gaver *et al.*'s (1990) estimate of $\mu \approx 10^{-1}\,\text{kg m}^{-1}\,\text{s}^{-1}$ gives a (more realistic) bubble propagation speed of $6\,\text{cm s}^{-1}$. In this high-viscosity scenario, steady airway reopening would be possible on the 'peeling' branch.

The three-dimensional model presented here is not without shortcomings. In particular, the effects of lung surfactant have been neglected by assuming a constant surface tension, σ^*. The transport of surfactant along the interface and its movement between the interface and the fluid will affect the local value of σ^* and hence the value of p_b^* at a given Ca (Yap & Gaver 1998). Inertial effects are also neglected in the present work, although they could be included without a major change in formulation. In two dimensions, Heil (2000) found that fluid inertia could lead to significant changes in the wall and interface shapes and caused an increase in p_b^* at any given capillary number. Finally, there is some question as to how well steady

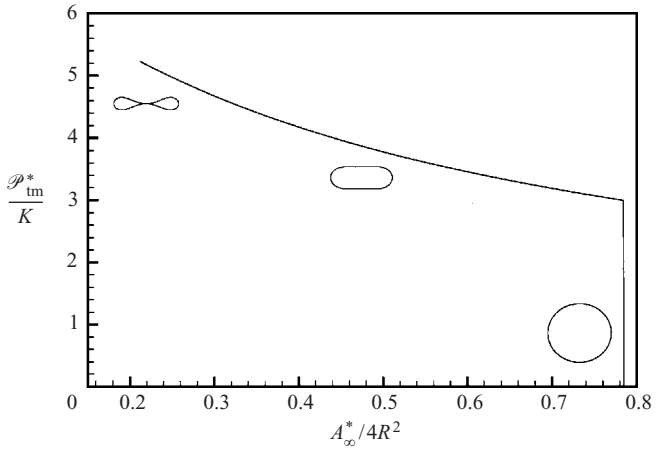

FIGURE 14. Variations in the cross-sectional area, A^*_∞, of an elastic tube under a uniform transmural pressure load, $\mathscr{P}^*_{\rm tm}$. Illustrative cross-sections are also shown and the final point on the graph is at opposite-wall contact, where $A_\infty \approx 0.21$.

reopening in an infinitely long straight tube approximates the physiological problem in the lung, where the liquid blockages are finite, the airway branches short and curved, and the motion unsteady, at least initially.

In response to this question, we refer to Cassidy, Gavriely & Grotberg (2001) recent experiments, which indicate that finite-length liquid plugs in dry straight tubes behave in a similar manner to semi-infinite plugs provided that the ratio of plug length to tube radius is greater than 20. Furthermore, after passage through a symmetric bifurcation, Cassidy *et al.* (2001) found that the behaviour of liquid plugs depends mainly upon the local plug *Ca*. Thus, apart from the motion through the bifurcation itself, the behaviour of the plug is adequately described by its behaviour in a single tube. We are therefore optimistic that the simplified model presented herein does indeed provide insight into the phenomena governing pulmonary airway reopening.

Financial support from the EPSRC is gratefully acknowledged. The HSL library routine MA42, a frontal solver for sparse unsymmetric systems, and the cfortran.h header file were used in the development of the numerical code in this work. The authors would also like to thank the anonymous referees for their helpful comments.

Appendix A. Thin-walled elastic tubes under uniform external pressure

Many aspects of bubble propagation in elastic tubes are a consequence of the tube's deformation under uniform pressure loading. Figure 14 shows the transmural (external minus internal) pressure, $\mathscr{P}^*_{\rm tm}$, as a function of the cross-sectional area, A^*_∞, of such a tube. The results were obtained by numerically solving equation (5) for a tube of length 10, subject to symmetry boundary conditions at $\zeta^1 = 0, 10$, and a loading term $f_i = \mathscr{P}_{\rm tm} N_i$.

At $\mathscr{P}_{\rm tm} = 0$, the tube is undeformed and the dimensionless cross-sectional area is $A^*_\infty/(4R^2) = \pi/4$. If $0 < \mathscr{P}_{\rm tm} < 3$, the tube remains axisymmetric with only a slight decrease in cross-sectional area. At $\mathscr{P}_{\rm tm} = 3$, there is a bifurcation to a non-axisymmetrically buckled shape and the area decreases rapidly with increasing external

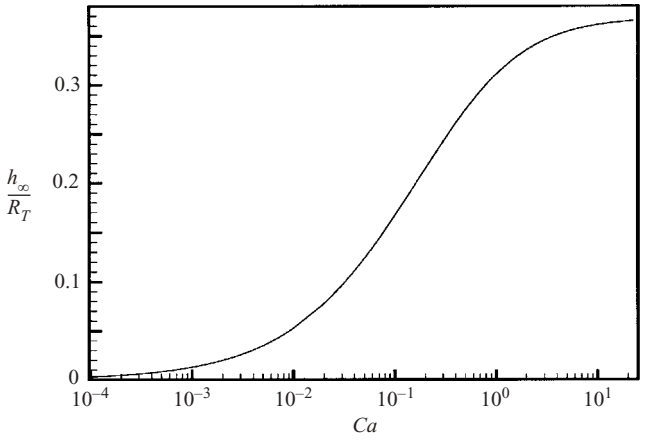

FIGURE 15. Dimensionless film thickness, h_∞/R_T, behind a semi-infinite air finger propagating into a fluid-filled rigid circular tube of radius R_T vs. capillary number.

pressure. Despite quite pronounced changes in tube geometry, the cross-sectional area is always a monotonically decreasing function of $\mathscr{P}_{\text{tm}}$.

On the axisymmetric branch, the external pressure may be related to the deformed tube radius, R_T, by the following (linearized) expression:

$$\frac{\mathscr{P}^*_{\text{tm}}}{K} = -(R_T - R)\,\frac{12}{(h/R)^2}. \tag{A 1}$$

For negative transmural pressures, $R_T > R$ and the tube will inflate axisymmetrically.

Appendix B. Bubble propagation in rigid circular tubes

Numerical results for the film thickness behind an air finger propagating into an axisymmetric tube filled with a viscous fluid have been presented by many authors (e.g. Reinelt & Saffman 1985; Giavedoni & Saita 1997). Figure 15 shows the film thickness as a function of capillary number from our finite element code for the propagation of air fingers in rigid tubes (Hazel & Heil 2002). As $Ca \to 0$, $h_\infty/R_T \to 0$ and as $Ca \to \infty$, $h_\infty/R_T \to C$, where $C \approx 0.36$.

Appendix C. The integral form of the governing equations

The finite element solution of the free-surface Stokes equations is based on their weak form. This is obtained by integrating the momentum equation (1*a*) over the fluid domain and using the tri-quadratic velocity shape functions, $\psi^{(F)}$, as test functions. The viscous and pressure-gradient terms are integrated by parts and the dynamic boundary condition (2*b*) is incorporated via the surface divergence theorem (Weatherburn 1955) to give

$$\int\int\int \left[p\frac{\partial \psi^{(F)}}{\partial x_i} - \left(\frac{\partial u_i}{\partial x_j} + \frac{\partial u_j}{\partial x_i}\right)\frac{\partial \psi^{(F)}}{\partial x_j}\right] \mathrm{d}V$$
$$+ \int\int \left[-pn_i + \left(\frac{\partial u_i}{\partial x_j} + \frac{\partial u_j}{\partial x_i}\right) n_j\right] \psi^{(F)}\, \mathrm{d}S_{\setminus S_{\text{fs}}}$$

$$+\frac{1}{Ca}\int\int\frac{1}{g}\,[\boldsymbol{g}_1]_i\left(g_{22}\frac{\partial\psi^{(F)}}{\partial s_1}-g_{12}\frac{\partial\psi^{(F)}}{\partial s_2}\right)+\frac{1}{g}\,[\boldsymbol{g}_2]_i\left(g_{11}\frac{\partial\psi^{(F)}}{\partial s_2}-g_{12}\frac{\partial\psi^{(F)}}{\partial s_1}\right)\mathrm{d}S_{\mathrm{fs}}$$
$$-\int\int p_b\psi^{(F)}n_i\,\mathrm{d}S_{\mathrm{fs}}-\frac{1}{Ca}\oint\psi^{(F)}m_i\,\mathrm{d}s=0. \qquad (\mathrm{C}\,1a)$$

The volume integrals are evaluated over the entire computational domain, V, and the surface integrals over the boundary of the domain, S, where $\boldsymbol{n}$ is the normal directed out of the bounding surface. S_{fs} is the free surface, paramaterized by the coordinates s_α and the covariant base vectors $\boldsymbol{g}_\beta$, $\beta=1,2$. $g_{\alpha\beta}\equiv\boldsymbol{g}_\alpha\cdot\boldsymbol{g}_\beta$ is the covariant metric tensor of the free surface and has the determinant g. The line integral is evaluated along the boundary of the free surface, where $\boldsymbol{m}$ is a unit vector tangent to the free surface and directed out of the domain.

The continuity equation (1b) is weighted by the tri-linear pressure shape functions $\psi^{(P)}$

$$\int\int\int\frac{\partial u_i}{\partial x_i}\psi^{(P)}\,\mathrm{d}V=0, \qquad (\mathrm{C}\,1b)$$

and the boundary condition (2a) is weighted by the bi-quadratic shape functions for the spine heights, $\psi^{(H)}$

$$\int\int u_i n_i\psi^{(H)}\,\mathrm{d}S_{\mathrm{fs}}=0. \qquad (\mathrm{C}\,1c)$$

A displacement-based finite element method is used to solve the shell equations (5) and hence the variations of the strain and bending tensors, $\delta\gamma_{\alpha\beta}$ and $\delta\kappa_{\alpha\beta}$, are taken with respect to the displacements, $\boldsymbol{v}$, and their derivatives with respect to the Lagrangian coordinates. In this work, we choose to resolve the displacement vector into components on the global Cartesian basis, rather than the undeformed basis of the shell, so that $\boldsymbol{v}=v^i\boldsymbol{e}_i$, where $\boldsymbol{e}_i$ is the unit vector in the x_i-direction. This representation (which differs from the one used in Heil 1997) is readily extendible to more general shell geometries and also reduces the algebraic complexity of the resulting variational equations, which become

$$\int_0^{2\pi}\int_{\zeta_S}^{\zeta_F}E^{\alpha\beta\gamma\delta}\Bigg(\gamma_{\alpha\beta}\boldsymbol{A}_\gamma\psi^{(S)}_{,\delta}+\frac{1}{12}\left(\frac{h}{R}\right)^2\kappa_{\alpha\beta}\left[\boldsymbol{N}\psi^{(S)}_{,\gamma\delta}+\frac{\boldsymbol{A}_2\times\boldsymbol{A}_{\gamma,\delta}}{\sqrt{A}}\psi^{(S)}_{,1}-\frac{\boldsymbol{A}_1\times\boldsymbol{A}_{\gamma,\delta}}{\sqrt{A}}\psi^{(S)}_{,2}\right.$$
$$\left.-\frac{\boldsymbol{N}\cdot\boldsymbol{A}_{\gamma,\delta}}{A}\left\{(A_{22}\boldsymbol{A}_1-A_{12}\boldsymbol{A}_2)\,\psi^{(S)}_{,1}+(A_{11}\boldsymbol{A}_2-A_{12}\boldsymbol{A}_1)\,\psi^{(S)}_{,2}\right\}\right]\Bigg)\sqrt{a}\,\mathrm{d}\zeta^1\,\mathrm{d}\zeta^2$$
$$=\frac{1}{12}\left(\frac{h}{R}\right)^3\frac{1}{1-\nu^2}\int_0^{2\pi}\int_{\zeta_S}^{\zeta_F}\left(\frac{R}{h}\right)\boldsymbol{f}\psi^{(S)}\sqrt{A}\,\mathrm{d}\zeta^1\,\mathrm{d}\zeta^2. \qquad (\mathrm{C}\,2)$$

Here, the extent of the finite computational domain is $\zeta_S\leqslant\zeta^1\leqslant\zeta_F$ and $\psi^{(S)}$ are the Hermite shape functions interpolating the displacements and their derivatives (Bogner *et al.* 1967).

Appendix D. Boundary conditions far ahead of the bubble tip: rigid vs. elastic tubes

In both rigid and elastic tubes, the propagating air finger deposits a stationary liquid film on the tube walls far behind the finger tip. Far ahead of the tip, fluid completely fills the tube and in order for the air finger to propagate some of this fluid must be displaced. In the case of the rigid tube, this can only be achieved by the

fluid being pushed into the tube ahead of the bubble. Therefore, the axial velocity far ahead of the bubble tip approaches a Poiseuille profile with a mass flux equal to the cross-sectional area occupied by the bubble far behind the tip.

In elastic tubes, the tube itself can deform to accommodate the passage of the bubble and there need not be any fluid motion far ahead of the tip. In fact, if there was any flow, the induced viscous pressure gradient would lead to an increase in transmural pressure, causing the tube to collapse more and more strongly with increasing axial distance. This would be inconsistent with the assumption that the tube's cross-sectional area approaches the (prescribed) value A_∞ as $x_3 \to -\infty$. The only possible steady-state travelling-wave solution is one in which $\partial p/\partial x_3 \to 0$ as $x_3 \to -\infty$. This implies that far ahead of the bubble tip the fluid velocity approaches a uniform profile, $u_3 = 1$ as $x_3 \to -\infty$ in the moving frame of reference.

REFERENCES

Bogner, F. K., Fox, R. L. & Schmit, L. A. 1967 A cylindrical shell discrete element. *AIAA J.* **5**, 745–750.

Bretherton, F. P. 1961 The motion of long bubbles in tubes. *J. Fluid Mech.* **10**, 166–188.

Cassidy, K. J., Gavriely, N. & Grotberg, J. B. 2001 Liquid plug flow in straight and bifurcating tubes. *Trans. ASME: J. Biomech. Engng* **123**, 580–589.

Cox, B. G. 1962 On driving a viscous fluid out of a tube. *J. Fluid Mech.* **14**, 81–96.

Duff, I. S. & Scott, J. A. 1996 The design of a new frontal code for solving sparse, unsymmetric linear systems. *ACM Trans. Math. Software* **22**, 30–45.

Flaherty, J. E., Keller, J. B. & Rubinow, S. I. 1972 Post buckling behavior of elastic tubes and rings with opposite sides in contact. *SIAM J. Appl. Maths.* **23**, 446–455.

Fry, D. L. 1968 Acute vascular endothelial changes associated with increased blood velocity gradients. *Circ. Res.* **22**, 165–197.

Gaver, D. P. III, Halpern, D., Jensen, O. E. & Grotberg, J. B. 1996 The steady motion of a semi-infinite bubble through a flexible walled channel. *J. Fluid Mech.* **319**, 25–56.

Gaver, D. P. III, Samsel, R. W. & Solway, J. 1990 Effects of surface tension and viscosity on airway reopening. *J. Appl. Physiol.* **369**, 74–85.

Ghadiali, S. N., Halpern, D. & Gaver, D. P. III 2001 A dual-reciprocity boundary element method for evaluating bulk convective transport of surfactant in free-surface flows. *J. Comput. Phys.* **171**, 534–559.

Giavedoni, M. D. & Saita, F. A. 1997 The axisymmetric and plane cases of a gas phase steadily displacing a Newtonian liquid – a simultaneous solution of the governing equations. *Phys. Fluids* **9**, 2420–2428.

Halpern, D. & Grotberg, J. B. 1992 Fluid-elastic instabilities of liquid-lined flexible tubes. *J. Fluid Mech.* **244**, 615–632.

Hazel, A. L. & Heil, M. 2002 The steady propagation of a semi-infinite bubble into a tube of elliptical or rectangular cross-section. *J. Fluid Mech.* **470**, 91–114.

Heil, M. 1997 Stokes flow in collapsible tubes: computation and experiment. *J. Fluid Mech.* **353**, 285–312.

Heil, M. 2000 Finite Reynolds number effects in the propagation of an air finger into a liquid-filled flexible-walled tube. *J. Fluid Mech.* **424**, 21–44.

Heil, M. 2001 The Bretherton problem in elastic-walled channels: Finite Reynolds number effects. In *IUTAM Symp. on Free Surface Flows* (ed. Y. Shikmurzaev), pp. 113–120. Kluwer.

Horsburgh, M. 2000 Bubble propagation in flexible and permeable channels. PhD thesis, Cambridge University.

Hughes, J. M. B., Rosenzweig, D. Y. & Kivitz, P. B. 1970 Site of airway closure in excised dog lungs: histologic demonstration. *J. Appl. Physiol.* **29**, 340–344.

Jensen, O. E., Horsburgh, M. K., Halpern, D. & Gaver, D. P. III 2002 The steady propagation of a bubble in a flexible-walled channel: asymptotic and computational models. *Phys. Fluids* **14**, 443–457.

Kistler, S. F. & Scriven, L. E. 1983 Coating flows. In *Computational Analysis of Polymer Processing* (ed. J. R. A. Pearson & S. M. Richardson), pp. 243–299. London: Applied Science Publishers.

Macklem, P. T., Proctor, D. F. & Hogg, J. C. 1970 The stability of the peripheral airways. *Respir. Physiol.* **8**, 191–203.

Pride, N. B. & Macklem, P. T. 1986 Lung mechanics in disease. In *Handbook of Physiology, Section 3: The Respiratory System*, Vol III, Part 2, pp. 659–692. American Physiological Society.

Reinelt, D. A. & Saffman, P. G. 1985 The penetration of a finger into a viscous fluid in a channel and tube. *SIAM J. Sci. Statist. Comput.* **6**, 542–561.

Taylor, C. & Hood, P. 1973 A numerical solution of the Navier–Stokes equations using the finite element technique. *Computers Fluids* **1**, 73–100.

Weatherburn, C. E. 1955 *Differential Geometry of Three Dimensions, Volume I*, 1st edn. Cambridge University Press.

Yamaki, N. 1984 *Elastic Stability of Circular Cylindrical Shells*. North-Holland.

Yap, D. Y. K. & Gaver, D. P. III 1998 The influence of surfactant on two-phase flow in a flexible-walled channel under bulk equilibrium conditions. *Phys. Fluids* **10**, 1846–1863.